

HCN SPECTROSCOPY OF COMET 73P/SCHWASSMANN–WACHMANN 3. A STUDY OF GAS EVOLUTION AND ITS LINK TO CN

L. PAGANINI^{1,6}, G. L. VILLANUEVA², L. M. LARA³, Z. Y. LIN³, M. KÜPPERS⁴, P. HARTOGH¹, AND A. FAURE⁵

¹ Max-Planck-Institut für Sonnensystemforschung, Max-Planck-Strasse 2, D-37191 Katlenburg-Lindau, Germany; lucas.paganini@nasa.gov

² Solar System Exploration Division, NASA Goddard Space Flight Center, Greenbelt, MD 20771, USA

³ Instituto de Astrofísica de Andalucía, CSIC, Camino Bajo de Huétor 50, 18008 Granada, Spain

⁴ European Space Astronomy Center (ESAC), P.O. Box 78, 28691 Villanueva de la Cañada, Madrid, Spain

⁵ Laboratoire d'Astrophysique de Grenoble (LAOG), Université Joseph-Fourier, UMR 5571 CNRS, BP 53, 38041 Grenoble Cedex 09, France

Received 2010 January 20; accepted 2010 April 14; published 2010 May 7

ABSTRACT

In 2006 May, comet 73P/Schwassmann–Wachmann 3 experienced large outburst activity allowing us to study the gas production rate of fresh material released from the nucleus. We observed the comet in a coordinated campaign using millimeter and optical facilities at heliocentric distances between 0.966 and 1.033 AU. During this time, we had the opportunity to follow the post-outburst evolution of fragment B, which evidenced larger production rates in comparison to fragment C, the latter showing a rather stable gas production rate ($Q_{\text{HCN}} \sim 2 \times 10^{25}$ molecules s^{-1}). In addition to the investigation of the gas evolution, we studied the possible role of HCN and dust as progenitors for the CN radical. From our joint observations on May 12, we observed a high correlation of CN with HCN and low correlation with the continuum emission (grains). Herewith, our study supports the view of HCN as a major source of CN, although the presence of other sources for cyanide cannot be fully ruled out.

Key words: astrochemistry – comets: general – comets: individual (73P/Schwassmann–Wachmann 3) – molecular processes – radiative transfer

Online-only material: color figures

1. INTRODUCTION

Cometary nuclei are considered primordial leftovers from the early time of our solar system, so the composition of their native ices represents comprehensive evidence of different thermochemical and physical conditions that occurred 4.6 billion years ago, the time when our planetary system was formed. Comets reside in two dynamical reservoirs: the Oort Cloud (source of nearly isotropic comets: long period and Halley type) and the Kuiper Belt (source of ecliptic comets: Jupiter-family comets, Encke type, and Centaur type). Individual comets from these reservoirs can be perturbed toward the inner solar system by various gravitational effects. As a comet approaches the Sun, volatile ices sublimate, and the ejected molecules can be spectroscopically detected, for instance, by observing their rotational or rovibrational transitions at submillimeter wavelengths.

The Jupiter-family comet 73P/Schwassmann–Wachmann 3 (hereafter 73P) constitutes one of the most relevant objects for cometary research. Discovered by Friedrich Carl Arnold Schwassmann and Arno Arthur Wachmann at the Hamburg Observatory in 1930, 73P is currently known for a large occurrence of outburst and defragmentation events. In particular, 73P broke up into several pieces during its perihelion passage in 1995. As a consequence, four fragments were observed and named alphabetically (Böhnhardt et al. 1995). The fourth one, however, was not seen elsewhere and thus might have been an ephemeral debris. In 2006, its close approach to Earth ($\Delta = 0.07$ AU) prompted astronomical observers to organize multiple observation campaigns using ground- and space-based facilities (e.g., Villanueva et al. 2006; Dello Russo et al. 2007; Fuse et al. 2007; Jones et al. 2008; Reach et al. 2009). During this time,

73P again experienced outbursts and nucleus defragmentation producing over three dozen pieces, which were observed before its perihelion passage. Clearly, the importance of these outburst episodes relies on the possibility of analyzing the fresh material in the coma which might thus enhance the study of intrinsic properties of cometary nuclei.

In 2006 May, we observed comet 73P/Schwassmann–Wachmann 3 using the 10 m Submillimeter Telescope. During this time, we had the unique opportunity to follow the post-outburst evolution of fragment B. Indeed, the advantage of radio spectroscopy relies on its capability to characterize the cometary coma and to determine, for instance, its chemical taxonomy, expansion velocities, kinetic temperatures, and production rates. Supporting observations with the 1 m telescope at the Lulin Observatory provided complementary information at optical wavelengths. The observed components were mainly fragments B and C focusing on molecular species, e.g., HCN, HNC, CH_3OH , CO, H_2CO , CS, CN, and the isotopic ratio $^{13}\text{N}/^{14}\text{N}$ in HCN. A complete report of the comet's chemical taxonomy will be presented elsewhere (G. L. Villanueva et al. 2010, in preparation). A previous study by Drahus et al. (2010) focused on the analysis of the rotation period of fragment C based on the analysis of short-term variabilities in HCN production rates. Among several plausible solutions for periodicity, a rotation period of 3.2 ± 0.2 hr was suggested to be the most likely.

In this publication, we seek to tackle two topics. First, we present the gas evolution of fragments B and C at heliocentric distances, r_h , from UT 2006 May 9 to May 22. This is performed by retrieving the gas production rates, kinetic temperature, and expansion velocity, using a recently developed analysis package called CERT, Cometary Excitation and Radiative Transfer (L. Paganini 2010, in preparation). CERT is a numerical code suitable for the simulation of emission lines at millimeter and

⁶ Present address: Solar System Exploration Division, NASA Goddard Space Flight Center, Mailstop 693.0, Greenbelt, MD 20771, USA.

submillimeter wavelengths in cometary comae, the latter including local thermodynamic equilibrium (LTE) and non-LTE conditions, i.e., collisions and radiative processes. The radiation process considers excitation of the HCN population distribution by absorption of solar photons via the ν_1 , ν_2 , $2\nu_2$, and ν_3 vibration bands. Second, we investigate the linkage between HCN and CN using our joint observations at millimeter wavelengths and CN imaging from the optical. Here, we analyze the consistency in production rates of HCN and CN, and further discuss the jet morphology in their radial distribution.

This paper is organized as follows. Section 2 details the instrumentation and observations. In Section 3, we give a short description of the excitation and radiative transfer code used during data analysis. The results of these observations and analysis, presented in Section 4, provide information regarding the gas production rates of HCN (Section 4.1) and CN (Section 4.2), and a comparison of jet morphologies between HCN mapping at millimeter wavelengths and CN images at optical wavelengths on 2006 May 12 (Section 4.3). Next, possible parent species for the CN radical are discussed in Section 5. Finally, Section 6 presents the conclusions for this work.

2. OBSERVATIONS

2.1. Submillimeter Wavelengths

Observations were performed with the Heinrich Hertz Submillimeter Telescope (HHSMT) between UT 2006 May 9 and 22. The telescope is located on Mt. Graham in southeast Arizona at an altitude of 3200 m (longitude W $109^\circ 53' 26''$, latitude N $32^\circ 42' 05''$). The HHSMT consists of a Cassegrain system with a paraboloidal main reflector and a hyperboloidal secondary reflector. The antenna has a diameter of 10 m, the absolute pointing accuracy is about $2''$, with a tracking accuracy of better than $1''$ (Baars et al. 1999); however, we have observed pointing errors of up to $\sim 8''$. The observations were performed using the dual polarization, single sideband 1.3 mm JT (130–300 GHz) and the dual-channel, double sideband MPIR SIS-345 receivers. The sensitivity of these instruments yielded mean system temperature (T_{sys}) of ~ 500 K during the observation campaign. The telescope is equipped with several back ends: (1) two chirp transform spectrometers (CTS) of (a) 218 MHz bandwidth (BW) 46.6 kHz spectral resolution (Δf) and (b) BW = 400 MHz Δf = 100 kHz; (2) a set of three acousto-optical spectrometers (AOSs), (a) AOS_A: Δf = 934 kHz, BW = 1 GHz, (b) AOS_B: Δf = 913 kHz, BW = 1 GHz, (c) AOS_C: Δf = 370 kHz, BW = 250 MHz; and (3) several filter banks.

We report astronomical observations of HCN species, transitions $J = 3-2$ ($\nu = 265886.1800$ MHz) and $J = 4-3$ ($\nu = 354505.4759$ MHz; Pickett et al. 1998). The half-power beamwidth (HPBW) for these transitions corresponds to $29''$ and $22''$, respectively. In this study, we use observations by the 218 MHz BW chirp transform spectrometer, which provides a velocity resolution of ~ 0.05 km s⁻¹ at $\nu = 250$ GHz. The spectral data are automatically calibrated by the telescope software into antenna temperature scale (T_A^*) using the chopper-wheel method (Ulich & Haas 1976). The observing mode for cometary observations was position switching (PS) which consists on pointing the telescope to the source (on-position) for an integration time of 15 s, and afterward the telescope is directed to the background (off-position) for a same integration time. A complete scan was finished after 5 minutes. After each 1 hr observing interval, observations of appropriate astronomical standard stars were acquired for pointing-accuracy determina-

tion and flux calibration. Afterward, the scanning procedure was repeated; i.e., the comet was observed again for 1 hr. Telescope tracking of the comet was computed using daily updated orbital elements from the JPL Horizons Ephemeris System⁷ (Table 1 shows the log of the observations). Main-beam efficiencies were attained from continuum observations of Venus, Mars, Jupiter, and Saturn, and line observations of G34.3, DR21, CRL2688, and W51d.

2.2. Optical Wavelengths

At optical wavelengths, our observations were obtained with the 1 m telescope at the Lulin Observatory, National Central University, Taiwan equipped with a PI1300B 1340×1300 CCD camera with an effective pixel scale of $0''.515$ pixel⁻¹ (Kinoshita et al. 2005). These observations were performed with the ESA Rosetta comet filter set for CN at 387/6 nm and the blue continuum at 445/4 nm (Table 2). The telescope tracking speed was set to the proper motion of the comet on the sky. The image data reduction has followed standard procedures which began with bias and dark current subtraction, and flat-field correction for all frames. The night sky contribution was subtracted from the comet images themselves at positions where no clear comet contribution was detected. This can easily be done for the images acquired with the BC filter as the dust coma does not fill the field of view (FOV). However, for the gas images, we estimated the sky contribution from the SW edge of the frame where no clear gas emission can be detected. The amount of sky background measured only represents 2% of the comet emission. We have used the spectrophotometric standard star BD+28D4211 for calibration into physical units. After every individual comet image is flux-calibrated, a final resulting comet image from the CN and the BC filters is obtained by median combining the complete CN and BC set of frames (see Lin et al. 2007 and 2009 for further details).

3. HCN EXCITATION AND RADIATIVE TRANSFER MODEL

A convenient method to determine the chemical taxonomy of comets—a classification based on the nature of ices and dust that comprise the nucleus—is to observe the parent volatiles (and refractory grains) shortly after their release from the cometary nucleus. As a comet approaches the Sun, the bulk composition of cometary nuclei can be analyzed by radio spectroscopy. The analysis of cometary comae by this method allows quantification of parent molecules with high spectral resolution.

Hydrogen cyanide is one of the best-studied molecules at radio wavelengths. Since the HCN molecule has a large dipole moment, and thus a short rotational lifetime, its LTE region is relatively small in the cometary coma. A proper extraction of their absolute production rates and mixing ratios (relative populations) from the measured line intensities requires a comprehensive investigation of the excitation processes and radiative transfer in the coma. As described by Crovisier (1984) and Weaver & Mumma (1984), the main excitation mechanisms within the cometary coma are collisions and radiative processes. In the first case, excitation involves collisions of the neutral gas with water vapor and electrons, controlling rotational populations in the inner coma, up to a cometocentric radius of 10^2 – 10^4 km depending on cometary activity (Xie & Mumma 1992). Radiative processes are important for excitation throughout the coma, but

⁷ <http://ssd.jpl.nasa.gov/?horizons>

Table 1
Log of Observations at Millimeter and Optical Wavelengths

	Date (2006 UT)	r_h (AU)	Δ (AU)	P.A. ^a (deg)	α^b (deg)	HCN (UT)	CN (UT)
Fragment B	May 9	1.033	0.078	229.9	70.5	10:54–12:18	...
	May 10	1.027	0.074	235.1	74.8	12:13–13:31	...
	May 11	1.020	0.070	240.4	79.5	15:19–15:36	...
	May 12	1.015	0.068	244.8	83.7	07:53–17:02	18:17–19:28
	May 17	0.990	0.072	256.1	105.1	09:45–19:20	...
	May 20	0.976	0.086	253.1	112.1	18:47–19:28	...
	May 21	0.973	0.091	251.9	113.0	10:35–19:50	...
Fragment C	May 9	1.027	0.083	242.1	75.3	06:32–15:42	...
	May 10	1.021	0.080	245.4	79.4	07:33–15:28	...
	May 11	1.015	0.079	248.8	84.2	15:55–17:04	...
	May 12	1.010	0.079	250.8	87.8	09:03–17:23	19:46–20:19
	May 17	0.986	0.090	253.8	104.1	11:31–16:55	...
	May 20	0.973	0.105	250.8	108.7	10:54–18:39	...
	May 22	0.966	0.117	248.6	110.0	10:59–12:15	...

Notes.

^a Solar position angle.

^b Solar phase angle.

they determine rotational populations only in the outer coma (i.e., beyond a cometocentric radius of 10^4 km), where there exists a balance (fluorescence equilibrium) between rovibrational levels absorbing solar radiation and the subsequent spontaneous decay into excited rotational levels in the ground vibrational state (which also experience radiative cooling).

Due to a larger FOV, numerical simulations of millimeter and submillimeter observations need to account for all excitation processes and non-LTE conditions within the coma. We have analyzed 73P data using a recently developed analysis package called CERT. CERT is a numerical code suitable for the simulation of emission lines at millimeter and submillimeter wavelengths in cometary comae, the latter including LTE and non-LTE conditions. In addition, CERT considers the actual heliocentric and geocentric distances of the comet and, if available, possible telescope offsets. Basically, the following points describe the different mechanisms composing this code.

First, a molecular excitation model considers spherically symmetric outflow to describe the spatial density distribution of parent species ejected from the nucleus (including their photodissociation rate). The radial density distribution is calculated for a large number of cells within the coma up to a cometocentric radius of 10^6 km extending equally in logarithmic space. The excitation characteristics within each cell are considered constant, and the molecular density is defined as

$$n_{\text{HCN}}(r) = \frac{Q_{\text{HCN}}}{4\pi r^2 v_{\text{exp}}} e^{-\frac{(r-r_0)}{\lambda_p}}, \quad (1)$$

where Q_{HCN} is the production rate, r is cometocentric radius, v_{exp} is the gas expansion velocity, r_0 is the nucleus radius (assumed to be 500 m for fragments B and C), and λ_p is the photodissociation scale length. λ_p is equal to $v_{\text{exp}}/\beta_{\text{HCN}}$, where $\beta_{\text{HCN}} = \beta_0/r_h^2$, and the dissociation rate at 1 AU heliocentric distance, β_0 , is $1.6 \times 10^{-5} \text{ s}^{-1}$ at solar minimum (Biver et al. 1999). Even though CERT handles temperature and velocity profiles (e.g., Crovisier 1984; Combi et al. 1999), we use constant values to describe the expansion velocity and kinetic temperature in the cometary coma.

A radiative transfer code is applied based on the existing accelerated Monte Carlo approach for star formation models

Table 2
Characteristics of the Observed Species

Species	Transition	Wavelength
HCN	3–2	1.13 mm
	4–3	0.85 mm
CN	$\text{B}^2\Sigma^+ - \text{X}^2\Sigma^+(0,0)$	387/6 nm
Dust	...	445/4 nm

by Hogerheijde & van der Tak (2000). This code has been adapted for cometary applications, similarly as by Bensch & Bergin (2004). Nevertheless, CERT uses a novel approach which greatly improves the overall execution speed of Monte Carlo methods by parallel processing using the Message Passing Interface (MPI).

The radiative transfer equation describes the emission, absorption, and motion of photons along a line in the direction of propagation, and is defined as

$$\frac{dI_\nu}{d\tau_\nu} = S_\nu - I_\nu, \quad (2)$$

where S_ν is the source function, I_ν represents the specific intensity of electromagnetic radiation, and $d\tau_\nu = \alpha_\nu ds$ the optical depth. In a two-level system, the molecular line transfer is determined by transition rates between two molecular rotational levels, i (upper) and j (lower), characterized by their specific population, n_i and n_j . The source function is thus given by $S_{ij}(\nu) = j_{ij}(\nu)/\alpha_{ij}(\nu)$, where $j_{ij}(\nu)$ and $\alpha_{ij}(\nu)$ stand for emission and absorption coefficients, given by

$$j_{ij}(\nu) = \frac{h\nu_o}{4\pi} n_i A_{ij} \phi(\nu), \quad (3)$$

$$\alpha_{ij}(\nu) = \frac{h\nu_o}{4\pi} (n_j B_{ji} - n_i B_{ij}) \phi(\nu). \quad (4)$$

The Einstein coefficients for spontaneous emission and absorption, A_{ij} and B_{ji} , and stimulated emission, B_{ij} , are obtained from a molecular line atlas. The function $\phi(\nu)$ describes the line profile function.

The relative level populations are obtained from the statistical equilibrium equation,

$$n_i \left[\sum_{j<i} A_{ij} + \sum_{j\neq i} (B_{ij} J_v + C_{ij} + G_{ij}) \right] = \sum_{j>i} n_j A_{ji} + \sum_{j\neq i} n_j (B_{ji} J_v + C_{ji} + G_{ji}), \quad (5)$$

which is solved by iteration, using matrix inversion and LU decomposition, until the solution has arrived to a satisfactory value (Hogerheijde & van der Tak 2000). J_v is the mean intensity, which is the integrated specific intensity from all solid angles, $d\Omega$. The collisional rate is $C_{ij} = n_{cp} k_{ij}$ with k_{ij} being the collision rate coefficients and n_{cp} the density of the collision partners. The contribution of radiative processes is determined by “effective” pumping rates G_{ij} (Bensch & Bergin 2004), using fluorescence models (in the CERT package).

The excitation of molecular rotational levels is modeled for collisions of hydrogen cyanide with water and electrons, using theoretical cross sections (σ). Since there are no detailed cross sections for water and hydrogen cyanide, i.e., relative to their rotational level properties, we have followed the standardized method of using a constant $\sigma_{\text{H}_2\text{O}-\text{HCN}}$ equal to $1 \times 10^{-14} \text{ cm}^2$ (Biver et al. 1999). Furthermore, the contribution of collisional excitation by thermal electron impact has been calculated using the molecular R -matrix method combined with the adiabatic-nuclei-rotation (ANR) approximation. We consider e -HCN rotation rates for transitions among all levels up to $J = 8$, and the fit of Faure et al. (2007) was employed up to $T = 10,000 \text{ K}$. The electron density and temperature profiles are derived from measurements in the coma of 1P/Halley following the study by Biver (1997); we use a scaling factor $x_{ne} = 0.3$.

The contribution of radiative processes to the line intensity is determined by detailed emission rates using a fluorescence model, the so-called g -factors. The calculation of g -factors is based on ab initio parameters, such as Einstein A -coefficients, statistical weights, and line strengths. The detailed pumping rate, due to the solar infrared radiation at a temperature $T_{bb} = 5770 \text{ K}$ and having solid angle Ω_{bb} , is

$$g_{ji} = \frac{\Omega_{bb}}{4\pi} P_j \frac{\omega_i}{\omega_j} A_{ij} \left(e^{\frac{hc\sigma_{ji}}{kT_{bb}}} - 1 \right)^{-1}, \quad (6)$$

where P_j is the rotational population of the lower level j , ω_i and ω_j are the statistical weights of the upper and lower levels, h is Planck’s constant, k is Boltzmann’s constant, c is the speed of light, and σ_{ji} is the frequency (see Crovisier & Encrenaz 1983 for further details).

CERT only considers cold (or fundamental) bands and accesses the HITRAN 2008 Molecular Line Atlas (Rothman et al. 2009) to obtain the required molecular parameters (which are attuned to the corresponding rotational temperature). Following Bockelée-Morvan et al. (1984), the radiation process considers excitation of the HCN population distribution by absorption of solar photons via the ν_1 , ν_2 , $2\nu_2$, and ν_3 vibration bands (accounting for 40 rotational levels), and the subsequent spontaneous decay into the excited rotational levels in the ground vibrational state. The l -type splitting of the $2\nu_2$ rotational levels was considered; however, hyperfine structures have been ignored. Excitation via ν_3 has been observed to be negligible. In addition, the outer coma is considered optically thin, so here any opacity effects have been neglected.

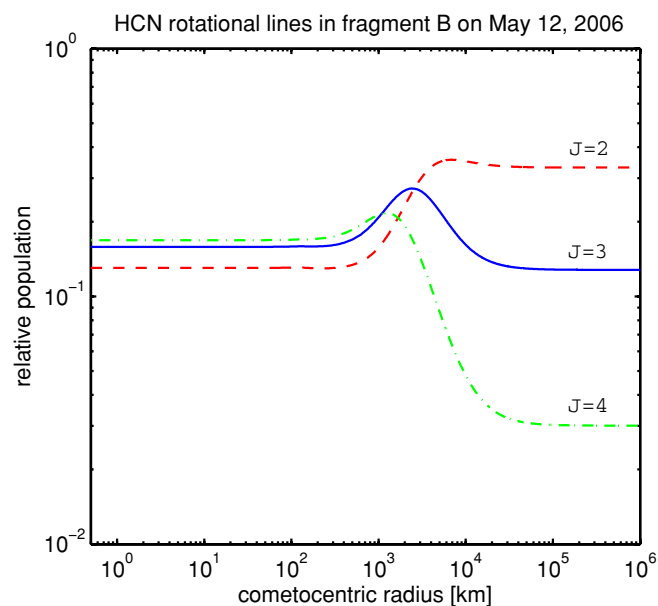


Figure 1. Level population of HCN corresponding to fragment B on 2006 May 12. This calculation considers: (1) a cometary coma extending from 500 m up to 10^6 km , (2) a constant kinetic temperature of 90 K, (3) interaction with water vapor and electrons, and (4) contribution of radiative processes of 40 rotational levels within vibrational bands ν_1 , ν_2 , $2\nu_2$, and ν_3 into the ground vibrational state.

(A color version of this figure is available in the online journal.)

Following Bensch & Bergin (2004), the effective pumping rate is computed from the detailed contribution of cascading rotational levels (g_{ij}), within the considered vibrational bands (i.e., ν_1 , ν_2 , $2\nu_2$, and ν_3), into each excited rotational level in the ground vibration state:

$$G_{ij} = \sum_{J',v'} g_{ij}(J', v'). \quad (7)$$

Figure 1 displays an example of the rotational population distribution corresponding to 73P-B on 2006 May 12 (cf. Figure 1 in Bockelée-Morvan et al. 2004). These level populations have been computed using a constant temperature along the coma equal to 90 K. We can observe an evolution from thermal to fluorescence equilibrium in the cometary atmosphere. The SMT FOV for the $J = 3-2$ rotational transition equals 1662 km and 1161 km for $J = 4-3$ (at their proper frequencies and $\Delta = 0.079 \text{ AU}$). These FOVs correspond to cometocentric radii of 831 and 581 km, respectively. Thus, we note that both FOV configurations are mostly sensitive to the inner coma where thermal equilibrium predominates. A temperature variation, however, is estimated to occur according to kinetic models (Crovisier 1984). This variation accounts for cooling due to gas adiabatic expansion close to the coma and a temperature increase due to solar heating at larger distances.

4. RESULTS

4.1. HCN Production Rates: Evolution of Cometary Outgassing

The measured HCN spectra were reduced using CLASS from the GILDAS software package.⁸ The synthetic HCN line emission is calculated after ray tracing using SKY (Hogerheijde

⁸ <http://www.iram.fr/IRAMFR/GILDAS>

Table 3
73P-B Production Rates

Molecule	Date (UT)	r_h (AU)	Δ (AU)	$\int T_b dv^a$ (K km s ⁻¹)	Q_{HCN} (10 ²⁵ s ⁻¹)	Q_{CN} (10 ²⁵ s ⁻¹)	$\frac{Q_{\text{HCN}}^b}{Q_{\text{H}_2\text{O}}}$ (%)
HCN(3–2)	May 9	1.033	0.078	0.96 ± 0.04
	May 11	1.020	0.070	2.40 ± 0.09	3.23 ± 0.25	...	0.17
	May 12	1.015	0.068	2.33 ± 0.06	3.04 ± 0.16	6.42 ± 0.74	0.16
	May 17	0.990	0.072	1.62 ± 0.10	2.21 ± 0.30	...	0.20
	May 20	0.976	0.086	0.90 ± 0.14	1.30 ± 0.44	...	0.20
	May 21	0.973	0.091	0.65 ± 0.05	0.97 ± 0.16	...	0.20
HCN(4–3)	May 10	1.027	0.074	7.11 ± 0.08	5.93 ± 0.15	...	0.31

Notes.

^a Line intensities are calculated using a velocity interval equal to ±1 km s⁻¹.

^b The water production rate is 1.9×10^{28} s⁻¹ on May 10–12 (from Kobayashi et al. 2007). Because of the large variability observed in fragment B at infrared wavelengths, we use a constant $Q_{\text{HCN}}/Q_{\text{H}_2\text{O}} = 0.2\%$ after May 12.

Table 4
73P-C Production Rates

Molecule	Date (UT)	r_h (AU)	Δ (AU)	$\int T_b dv^a$ (K km s ⁻¹)	Q_{HCN} (10 ²⁵ s ⁻¹)	Q_{CN} (10 ²⁵ s ⁻¹)	$\frac{Q_{\text{HCN}}^b}{Q_{\text{H}_2\text{O}}}$ (%)
HCN(3–2)	May 9	1.027	0.083	1.30 ± 0.02	2.20 ± 0.07	...	0.19
	May 11	1.015	0.079	1.23 ± 0.06	1.97 ± 0.22	...	0.17
	May 12	1.010	0.079	1.13 ± 0.04	1.83 ± 0.13	2.06 ± 0.34	0.16
	May 17	0.986	0.090	1.05 ± 0.06	1.90 ± 0.22	...	0.17
	May 20	0.973	0.105	0.91 ± 0.04	1.86 ± 0.18	...	0.16
	May 22	0.966	0.117	1.21 ± 0.10	2.74 ± 0.46	...	0.24
HCN(4–3)	May 10	1.021	0.080	2.06 ± 0.05	2.09 ± 0.11	...	0.18

Notes.

^a Line intensities are calculated using a velocity interval equal to ±1 km s⁻¹.

^b The water production rate is 1.14×10^{28} s⁻¹ (from Dello Russo et al. 2007), assumed to be constant over the whole observation campaign.

& van der Tak 2000) and later analyzed with the MIRIAD package (Sault et al. 1995). The resulting HCN brightness distribution is convolved with a beam of 29'' for the $J = 3-2$ and 22'' for the $J = 4-3$, which are the representative HPBW's of the Submillimeter Telescope at their corresponding frequencies. Next, a power-law fit obtains an equation for simulated production rates as a function of synthetic line-integrated intensities. Afterward, the HCN production rate is retrieved from this derived equation by introducing the observed line-integrated intensities.

Production rates have been estimated from heliocentric distances between 0.966 and 1.033 AU before perihelion. An expansion velocity, v_{exp} , of 0.53 km s⁻¹ and a kinetic temperature of 90 K were retrieved for 73P-B. Accordingly, determination of these values for fragment C yielded a v_{exp} of 0.63 km s⁻¹ and $T_{\text{kin}} = 65$ K. Tables 3 and 4 summarize results from HCN observations using HHSMT. An example of observed and modeled spectra on May 12 is given in Figure 2. Our procedure is to use water production rates, $Q_{\text{H}_2\text{O}}$, obtained by direct IR observations of water hot bands. In the case of 73P-B, we note that water production estimations at IR wavelengths vary largely, so a constant value of 1.9×10^{28} s⁻¹ is assumed (from Kobayashi et al. 2007; Bonev et al. 2008a); on May 9, the $Q_{\text{H}_2\text{O}}$ was reported to be 3.5×10^{28} s⁻¹. In the same way, we employ a mean $Q_{\text{H}_2\text{O}}$ of 1.14×10^{28} s⁻¹ for fragment C (Dello Russo et al. 2007).

Our observation coverage allows us to infer on the outgassing evolution of fragments B and C at millimeter wavelengths. As observed in Figure 3, a strong decrease of gas production of

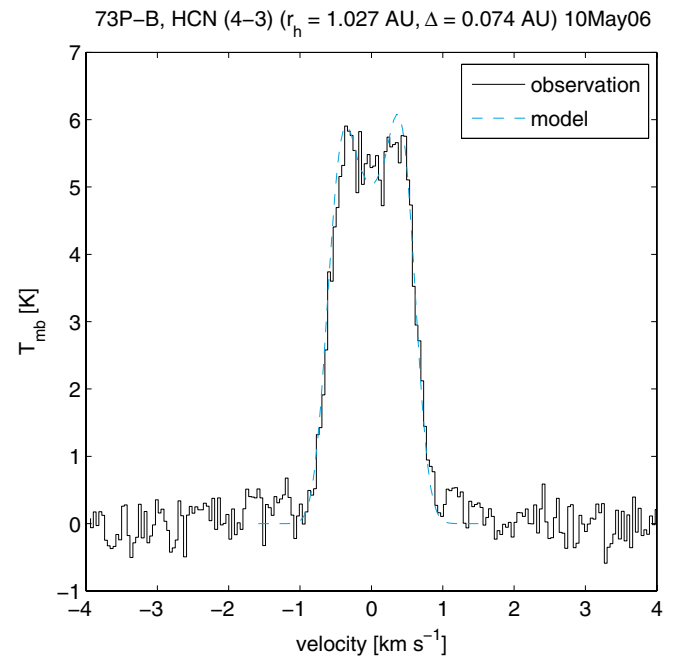


Figure 2. HCN (4–3) emission line of 73P/Schwassmann–Wachmann 3 fragment B on 2006 May 10. Black: observed spectrum, blue dashed: model result.

(A color version of this figure is available in the online journal.)

73P-B is confirmed from our observations on May 10. Existing calculations of HCN production rates in fragment B on May

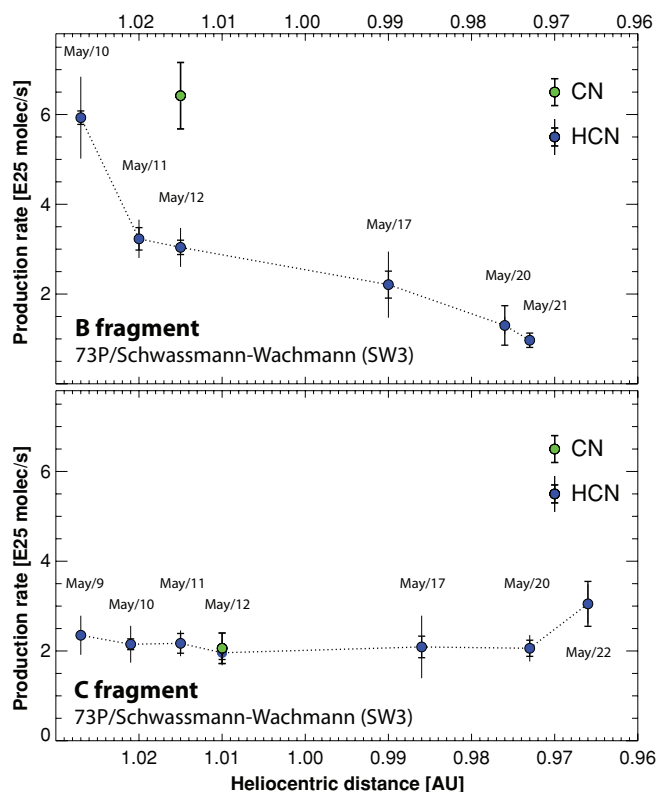


Figure 3. Production rate evolution for fragments B and C during the observational campaign. Values retrieved from the submillimeter data for HCN are presented with blue dots, and values for CN (retrieved from the optical) are presented with green dots. Stochastic uncertainties (associated with the intrinsic signal-to-noise ratio of the data) are drawn with horizontal error bars, while the systematic uncertainties are described with vertical lines. Systematic errors are introduced by transient weather conditions and were quantified by frequently measuring flux standards, and retrieving the maximum excursions in the observed fluxes.

(A color version of this figure is available in the online journal.)

10–11 (Lis et al. 2008) are similar to our estimations. It is worth noticing a decrease of 73P-B's gaseous productivity by a factor of 2 in about a week as shown by our observations. These results evidence the rapid decrease in gas productivity after the outburst event which was already noticed by observations at other wavelengths (e.g., Dello Russo et al. 2007; Bertini et al. 2009). Indeed, during the period of May 10–17, fragment B evidenced larger production rates in comparison to 73P-C, the latter showing a rather stable gas production in its trajectory toward the Sun. Subsequent observations of 73P-B after May 17 ($r_h = 0.990$ AU) resulted in a lower gas productivity than that of fragment C.

In particular, Figure 4 shows the resulting spectrum from observations of 73P-B on May 9. Its strong asymmetry might be the result of an outgassing jet expanding in a direction away from the observer (Earth). Clearly, a three-dimensional (3D) model is eventually required to model such an event.

4.2. CN Production Rates

To obtain the pure gas emission profiles from the images acquired with the CN cometary filter, it is necessary to subtract the contribution of the underlying continuum, and the way to get the continuum contribution in the gas filter can be found in detail in Lin et al. (2007). The CN acquired images have 27.88% and 27.55% contributions of continuum in the blue range for B and C fragments, respectively. Therefore, the CN comet images

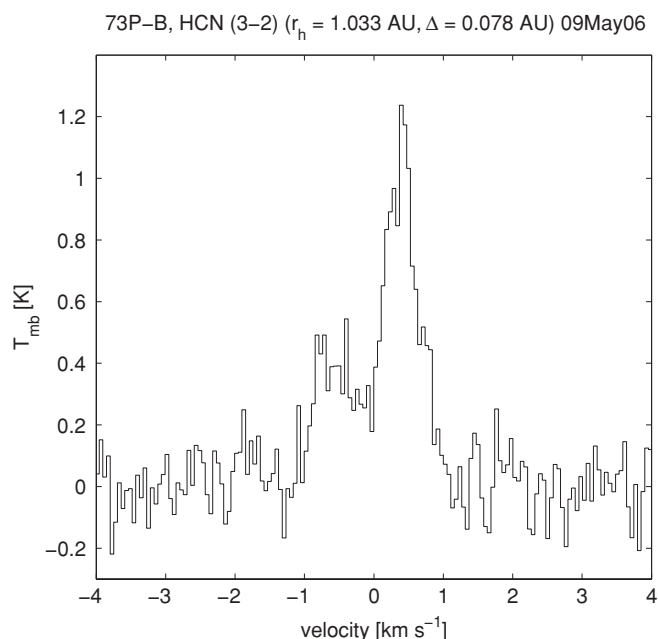


Figure 4. HCN(3–2) emission line of 73P/Schwassmann–Wachmann 3 fragment B obtained at the HHSMT on 2006 May 9.

result from the subtraction of the flux-calibrated images acquired with the CN cometary filters and the BC continuum images multiplied by the above-mentioned values ($\text{CN} \approx \text{CN}_{\text{obs}} - 0.28 \text{BC}_{\text{obs}}$). In order to determine gas production rates by means of the Haser model (Haser 1957), we have obtained a radial emission profile of CN from the images at a position angle (P.A.) where no clear structure is found, and where the projected cometocentric distance is maximum (i.e., southern hemisphere). Unfortunately, the position of the optocenter, usually centered at the comet nucleus, was located in the upper left corner of the CCD frame. This prevented us from obtaining full radial profiles by azimuthal average over 360° , as these profiles would only reach a projected cometocentric distance of ~ 4000 km. Such a distance is rather meaningless when applying the Haser model, and thus this clearly represents an undesired limitation in the optical data. On the one hand, we have a good spatial resolution but, on the other hand, a short spatial coverage given by a very short geocentric distance and small CCD.

In order to derive the CN production rate for both fragments, we have compared the observed density radial profile of CN with the theoretical curve of the Haser model, assuming $v_p = 0.53$ km s $^{-1}$ and 0.63 km s $^{-1}$ for fragments B and C, respectively (obtained from our millimeter observations), customary values for the daughter velocity v_d set to 1 km s $^{-1}$, and parent and daughter scale lengths $l_p = 13,000$ km and $l_d = 210,000$ km (from A'Hearn et al. 1995), respectively. Fluorescence efficiency factors for CN have been computed at the corresponding heliocentric distance and velocity from tabulated values in Schleicher (1983). We have considered a radial profile at P.A.s of $206^\circ.4$ and $200^\circ.8$ counted from north (up in the frames) toward east (left in the frames) for B and C fragments, respectively. This allows us to obtain radial profiles of CN column densities reaching a (maximum) projected cometocentric distance, ρ_{max} , of $11,700$ for fragment B and $14,000$ km for fragment C. Figure 5 shows the observed CN profile for B and C fragments together with the best fit by means of the Haser model. This best fit is obtained with $Q_{\text{CN}} = (6.42 \pm 0.74) \times 10^{25}$ s $^{-1}$ for fragment B and $(2.06 \pm 0.34) \times 10^{25}$ s $^{-1}$ for fragment C.

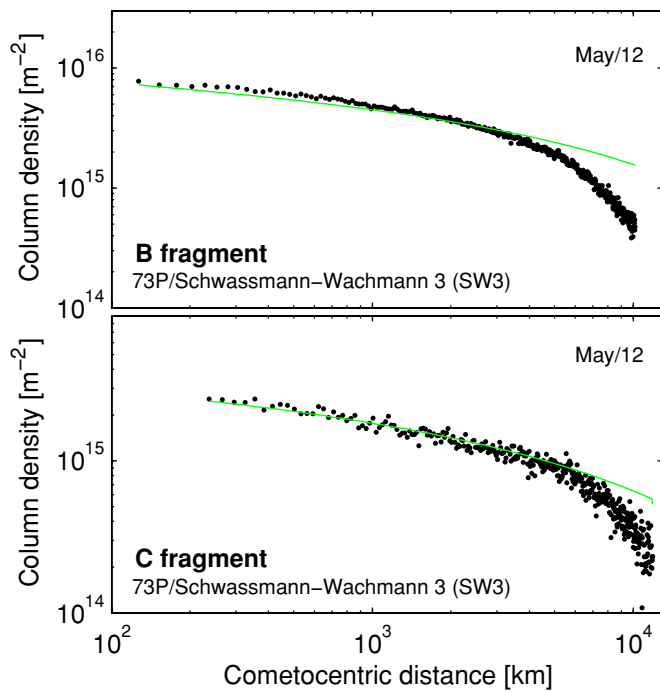


Figure 5. Observed CN profile for fragments B and C (black), along with the best fit by means of the Haser model (green).

(A color version of this figure is available in the online journal.)

4.3. Mapping of HCN: Comparison to Optical Images

Mapping of rotational emission lines has been only attempted in few comets (e.g., see Wright et al. 1998; de Pater et al. 1998; Blake et al. 1999; Lovell et al. 1999; Wink et al. 1999; Biver et al. 1999; Veal et al. 2000; Boissier et al. 2007). Position-switched mapping (PSM), which consists in moving the telescope beam across the source at a constant velocity, provides extended coverage of the molecular emissions with single-dish telescopes. On 2006 May 12, there was a unique opportunity to map the HCN molecule distribution in fragments B and C. Such spectral distribution maps were constrained by observing fragments B and C at different right ascension (R.A.) and declination (decl.) offsets from their central position. In particular, these observations were carried out during the comet's closest approach to Earth, which coincided with the period of outburst activity in fragment B (see Figure 6). As a result, additional information could be obtained on the spatial distribution by observing the line shapes projected along the line of sight (although with a limited spatial resolution of $\sim 10''$ at most).

For these observations, the orbital parameters for 73P-B were $r_h = 1.015$ AU, $\Delta = 0.068$ AU, the comet's elongation angle (ϕ ; Sun–Earth–comet) = 92° , comet's phase angle (α ; Sun–comet–Earth) = 84° , the solar P.A. of the extended radius vector = 245° , and the minus velocity vector (PsAMV) = 317° . Accordingly, orbital parameters for 73P-C were $r_h = 1.010$ AU, $\Delta = 0.079$ AU, $\phi = 88^\circ$, $\alpha = 88^\circ$, P.A. = 251° , and PsAMV =

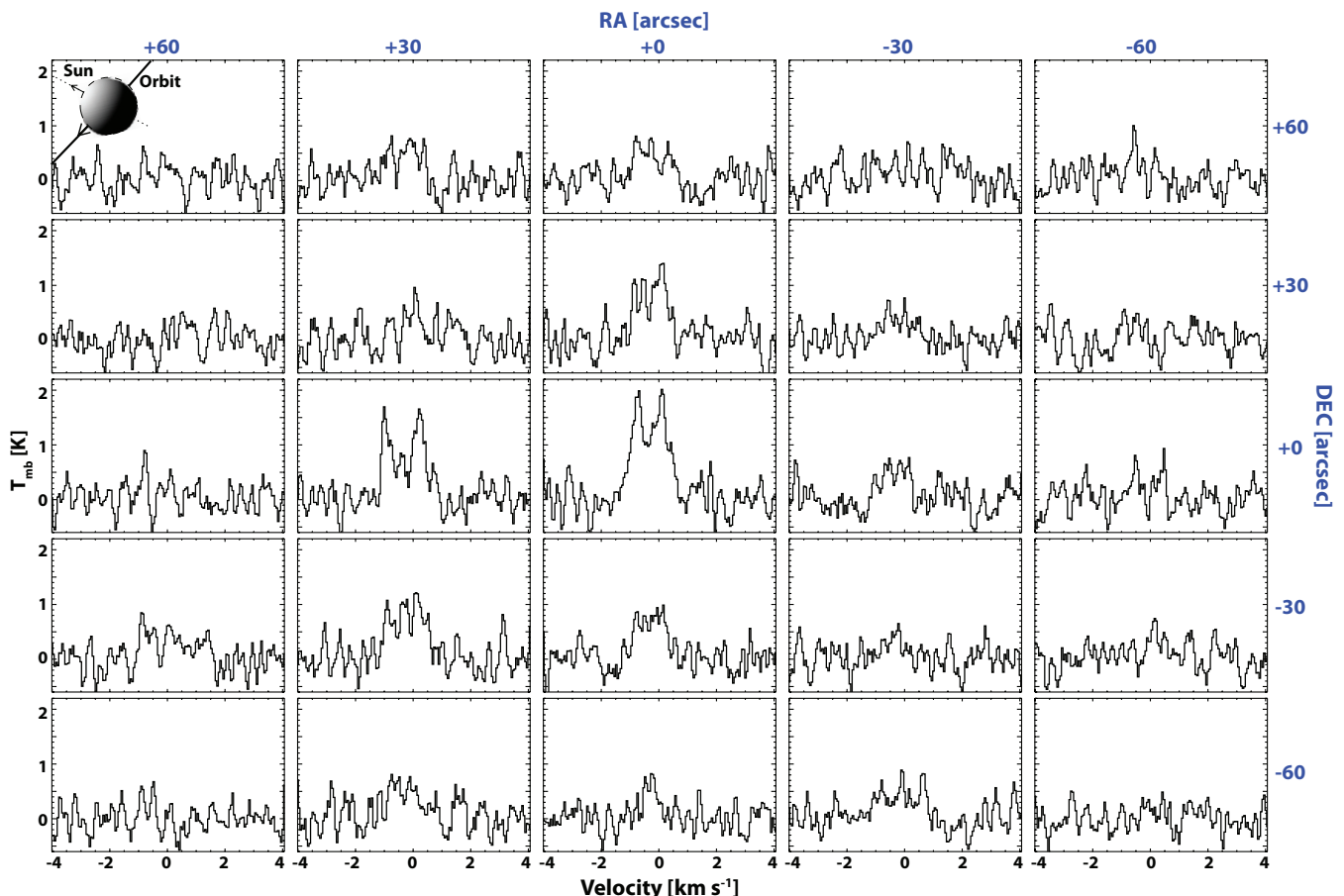


Figure 6. Spectral map of the HCN(3–2) emission line of comet 73P-B/Schwassmann–Wachmann 3 on 2006 May 12, using the PSM technique.

(A color version of this figure is available in the online journal.)

322°. Fragment B was observed between 12:25 and 14:50 UT and fragment C between 9:17 and 11:40 UT.

Despite the fact that PSM involves shorter integration times and thus less signal-to-noise ratios (S/Ns), fragment B displayed strong emission lines on May 12 which permitted maps with an FOV of $120'' \times 120''$. An interesting outcome from this map (see Figure 7 (top)) is that fragment B evidenced significant ejection in the SE direction and, to a less degree, toward the NW orientation—a distribution somewhat unusual since outburst events have been usually reported to appear in solar and anti-solar directions. This means that a main outburst was clearly evolving in the direction of motion of the B fragment during this day. Taking into account the lack of spatial resolution of millimeter mapping, this morphology agrees with arc structures reported by optical observers on previous days (Vincent et al. 2010).

Evidencing less gas production on the same day, fragment C was mapped with an FOV equal to $60'' \times 60''$ (see Figure 8 (top)). Its millimeter map suggests outgassing features in a three-axis configuration, i.e., toward the Sun position and a two-fold SE–NW elongation.

Comparison to optical images (bottom plots in Figures 7 and 8), with the same FOV and using the median algorithm to erase star traces, shows similar structures as those observed for HCN in millimeter maps. Moreover, we have used the adaptive Laplace filtering and the radial renormalization techniques to enhance any structure deviating from spherical symmetry in the gas and dust coma. As observed in Figures 9 and 10, the adaptive Laplace filtering also brings out the previously mentioned structures of CN. Similarly, the radial renormalization technique confirms the features found by Laplace filtering. We observe a low correlation between CN outgassing and the continuum images, i.e., the dust tail which heads toward the anti-solar direction (see bottom plots in Figures 9 and 10).

5. DISCUSSION ON HCN–CN PARENTAGE

The closest approach of 73P/Schwassmann–Wachmann 3 to Earth (before perihelion) gave us a unique opportunity to sample its inner coma and, thanks to the high spectral sensitivity of our submillimeter observations and a good spatial resolution of optical data, the chance to analyze particular outgassing features and characteristics close to the nucleus. In this section, we comment on jet morphologies and production rates from our joint observation on 2006 May 12, and further explore the possible role of HCN and dust as parents for CN.

Having a branching ratio of 97%, photodissociation of HCN leads to direct formation of H and CN (Huebner et al. 1992). As a result, hydrogen cyanide has been claimed as the major parent species for cometary cyanide. This affirmation, however, is a subject of extensive debate. The controversy started after determination of HCN/CN abundances in comet IRAS–Araki–Alcock (1983d), when Bockelée-Morvan et al. (1984) measured a lower HCN production rate than that corresponding to CN. This motivated Bockelée-Morvan et al. (1985) to propose additional parent sources for cometary CN, such as HC_3N , CH_3CN , and C_2N_2 . Formation via HC_3N or CH_3CN photodissociation has been shown to be minor since their production rates in C/1995 O1 (Hale–Bopp) were determined to be a factor of 10 lower than that of HCN (Bockelée-Morvan et al. 2000). The case of C_2N_2 , however, remains still inconclusive since its detection in comets has not been possible from current ground-based telescopes (due to the lack of sensitivity to detect its weak vibrational lines at infrared wavelengths).

According to Woodney et al. (2002), there exist three conditions to confirm HCN as the sole source for CN, these are as follows: (1) consistency in the production rate of HCN and CN, (2) agreement between the HCN photodissociation scale length and the observed CN parent scale length, and (3) a similar morphology in their radial distribution (although simultaneous investigation of all three conditions seems difficult to be accomplished.). For instance, Woodney et al. (2002) found a better correlation between HCN and CN than between HCN and the optically dominant dust in comet Hale–Bopp. Likewise, using the Berkeley–Illinois–Maryland Association (BIMA) array, Friedel et al. (2005) determined a consistent HCN production rate relative to that of CN in comet LINEAR (C/2002 T7). However, a similar analysis in comet NEAT (C/2001 Q4) resulted in lower HCN production rates, which suggested a different parent species for cyanide. Fray et al. (2005) derived an average value of CN parent scale lengths, considering minimum solar activity at a heliocentric distance of 1 AU, and compared HCN and CN production rates in several comets. From a total of eight comets, they found a correlation between HCN and CN production rates in one-half of the total samples only. Therefore, they concluded that an additional process is needed to explain the CN density observed in the remaining ones.

A particular case is that of comet 8P/Tuttle where, according to measurements using NIRSPEC at the Keck Observatory, Bonev et al. (2008b) claimed that HCN does not appear to be the native precursor for CN. Such a result has been indicated also by Waniak et al. (2009), who suggested a dust source as a potential formation mechanism for CN species. Origin of CN from dust particles has already been observed by Newburn & Spinrad (1989) and A'Hearn et al. (1995); however, the large variation among the sampled comets has denoted that formation from grains may not occur in all comets.

Investigation of HCN and CN isotopic ratios in comet C/1995 O1 (Hale–Bopp) has suggested a different source for CN (Manfroid et al. 2005). However, a revised analysis of Hale–Bopp's data plus recent determinations in comet 17P/Holmes have resulted in similar HCN and CN isotopic ratios (Bockelée-Morvan et al. 2008). Thus, Bockelée-Morvan et al. (2008) concluded that HCN is the main parent for CN in cometary comae.

Synchronous mapping at multiple wavelengths is a potential tool which is starting to take importance. Even though mapping at millimeter wavelengths has already been pursued by several astronomical observers, its synergy to address the HCN–CN parentage by means of comparison to other wavelengths has not yet been fully explored. On a previous attempt, Woodney et al. (2002) observed HCN jets in comet Hale–Bopp and combined them with near simultaneous CN images. The potential of this technique led them to observe similarities on production rates and radial distributions of HCN and CN, but discrepancies between scale lengths. As a result, the correlation between HCN and CN was certainly not perfect.

After comparing millimeter maps and optical images, we evidence a high reciprocity on jet morphologies of HCN and CN in fragment B (see Figure 7). Likewise, fragment C denotes a similar outcome (Figure 8). Their correlation is, however, not optimally attained forbidding us to establish any definite conclusion. In addition, we clearly observe the dust tail heading to the anti-solar direction in both fragments, which suggests a low correlation between CN outgassing and a grain source (see Figures 9 and 10). Thereby, dust does not seem to be an effective

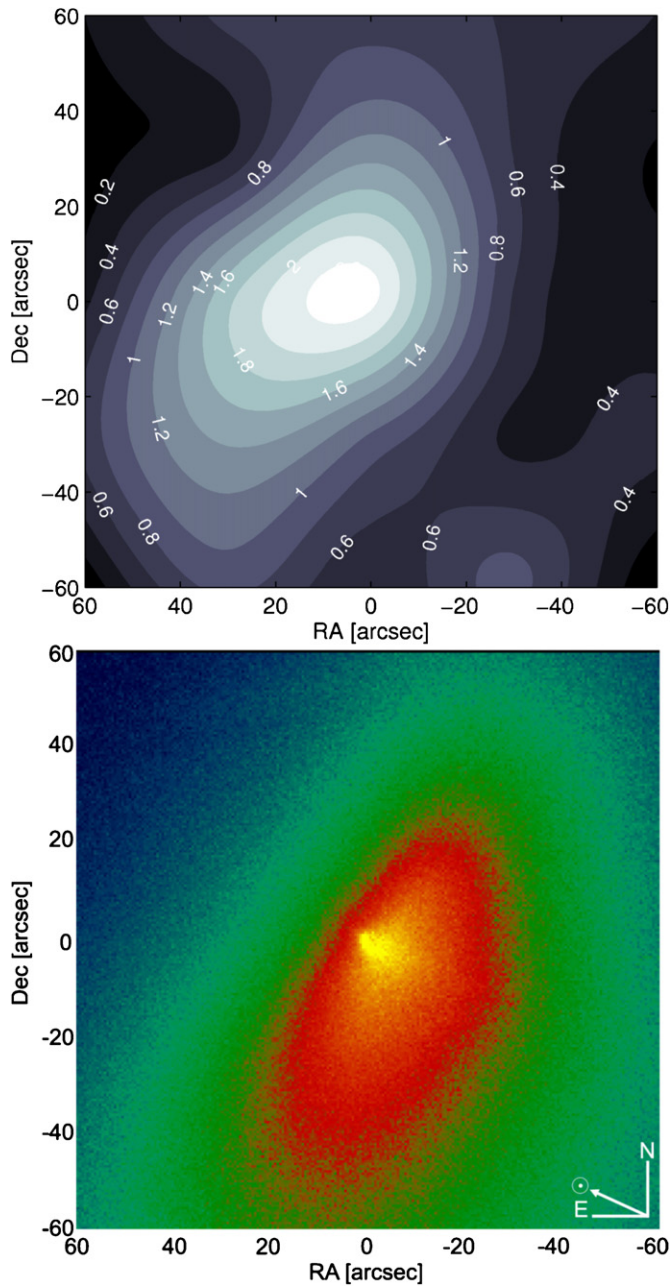


Figure 7. Comparison between HCN and CN features in fragment B on 2006 May 12. Top: spectral map of the HCN(3–2) emission line using the 10 m telescope at HHSMT (contours represent line-integrated intensities (K km s^{-1})). Bottom: optical images using the 1 m telescope at the Lulin Observatory (optical observations were performed with the ESA Rosetta comet filters for CN at 387/6 nm). The FOV is $120'' \times 120''$, corresponding to $\sim 6000 \times 6000$ km. (A color version of this figure is available in the online journal.)

source of CN in comet 73P, though a minor contribution should not be disregarded.

These millimeter maps are treated as snapshots of the cometary coma, but the time required to complete a map was in the order of 2.3 hr. The strong rotational variability claimed by Drahus et al. (2010) would suggest undesired effects in the brightness distribution when comparing distant points in the coma, i.e., artificial coma structures induced by nucleus rotation. On the other hand, a similar distribution of the coma morphology for HCN and CN in each fragment (Figures 7 and 8) would be an argument in favor of a real spatial variation as opposed to a dominating temporal/rotation effect.

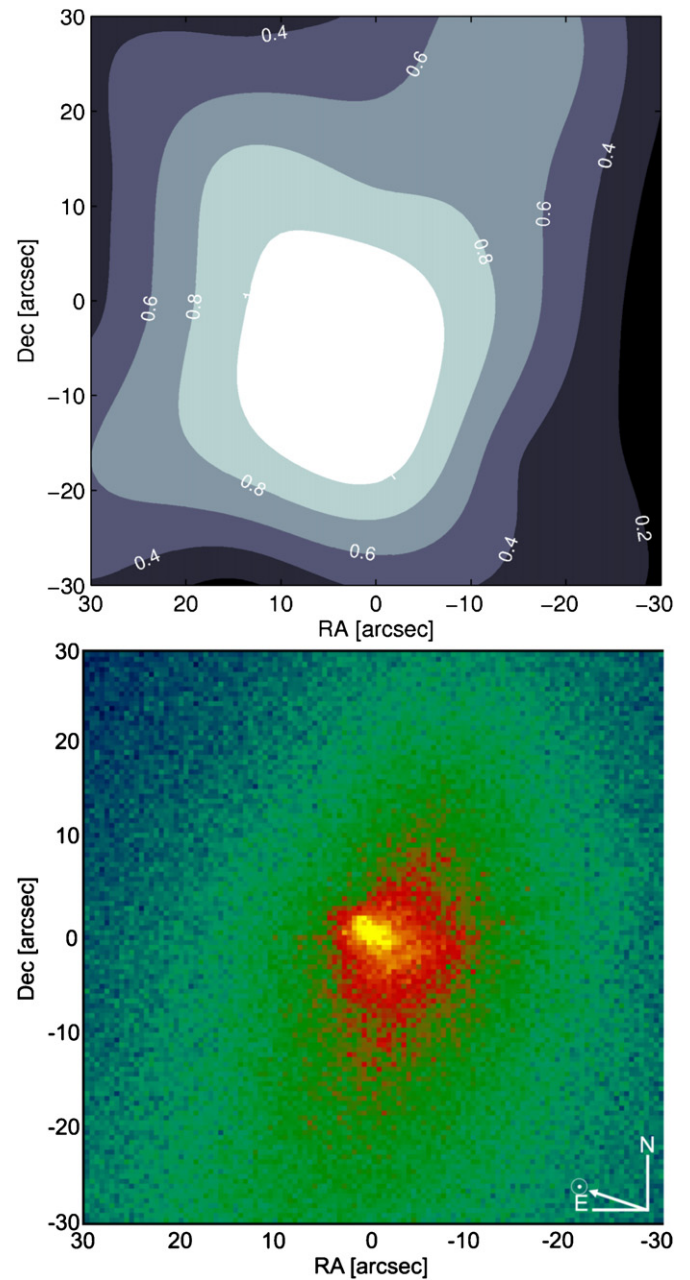


Figure 8. Comparison between HCN and CN features in fragment C on 2006 May 12. Top: spectral map of the HCN(3–2) emission line using the 10 m telescope at HHSMT (contours represent line-integrated intensities (K km s^{-1})). Bottom: optical images using the 1 m telescope at the Lulin Observatory. The FOV is $60'' \times 60''$, corresponding to $\sim 3500 \times 3500$ km. (A color version of this figure is available in the online journal.)

Concerning production rates, we have obtained Q_{HCN} equal to $(3.04 \pm 0.16) \times 10^{25} \text{ s}^{-1}$ (Section 4.1) and Q_{CN} resulted in $(6.42 \pm 0.74) \times 10^{25} \text{ s}^{-1}$ (see Section 4.2) for fragment B. In the case of fragment C, Q_{HCN} equals $(1.83 \pm 0.13) \times 10^{25} \text{ s}^{-1}$ and Q_{CN} is $(2.06 \pm 0.34) \times 10^{25} \text{ s}^{-1}$. Thus, comparison of HCN and CN production rates in fragment C indicates a mean value of Q_{CN} slightly larger than Q_{HCN} , if we bear in mind the estimated error bars and standard uncertainties these rates confirm hydrogen cyanide as the main source for the CN radical. In the case of fragment B, it is evident that CN production exceeds that of HCN by a factor of 2. However, it is important to mention that direct comparison of HCN and CN production

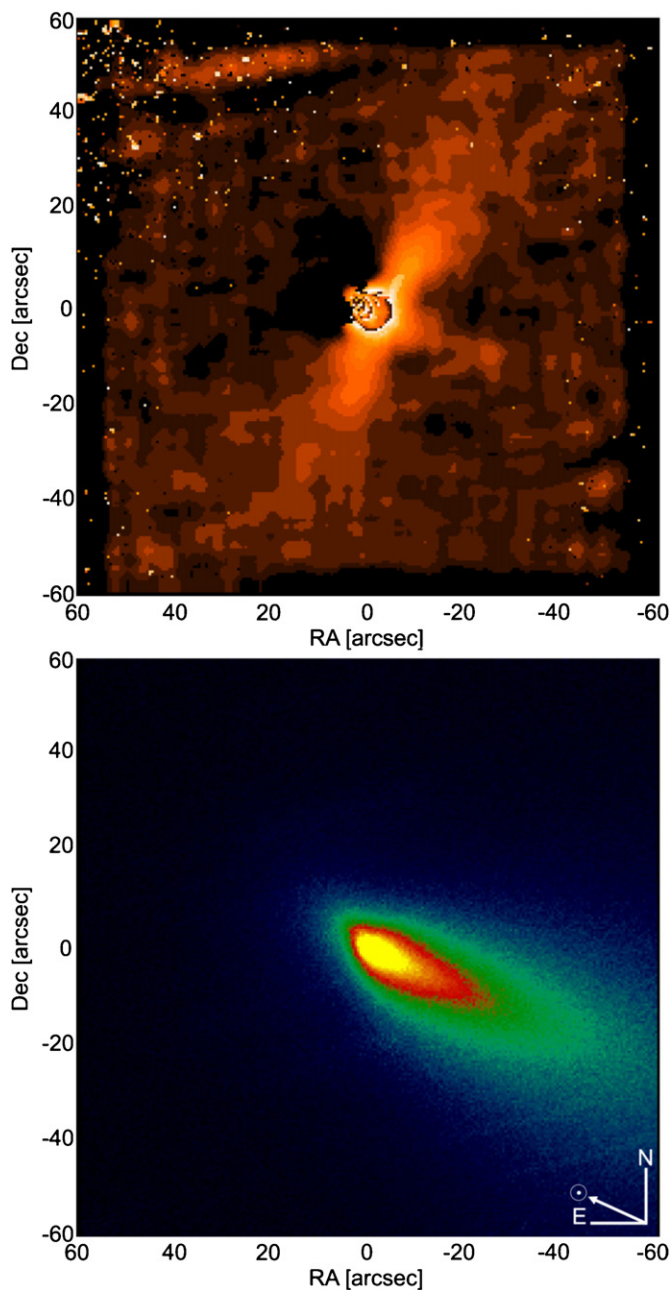


Figure 9. Comparison between CN structures and dust in fragment B. Top: adaptive Laplace filtering method of the CN image in Figure 7 (bottom). Bottom: optical images using the ESA Rosetta comet filters for the blue continuum at 445/4 nm.

(A color version of this figure is available in the online journal.)

rates is ill-conditioned. In order to derive production rates, we have assumed spherically symmetric outflow and steady production over the lifetime of the parent volatile. Similar to the impact event on comet Tempel 1, the rapid decrease in spectral intensity produced by outburst activity in fragment B demonstrates that steady-state production was not achieved, and thus these production rates should be interpreted as indicators of activity (Mumma et al. 2005). Moreover, the daughter scale length of 210,000 km corresponds to a timescale of ~ 2.4 days for the $\text{CN} \rightarrow \text{C} + \text{N}$ dissociation, i.e., CN measures the production rate at a slightly different time than HCN, and much of the CN observed on May 12 may still be from the HCN outburst on previous days. A time-dependent model (as opposed

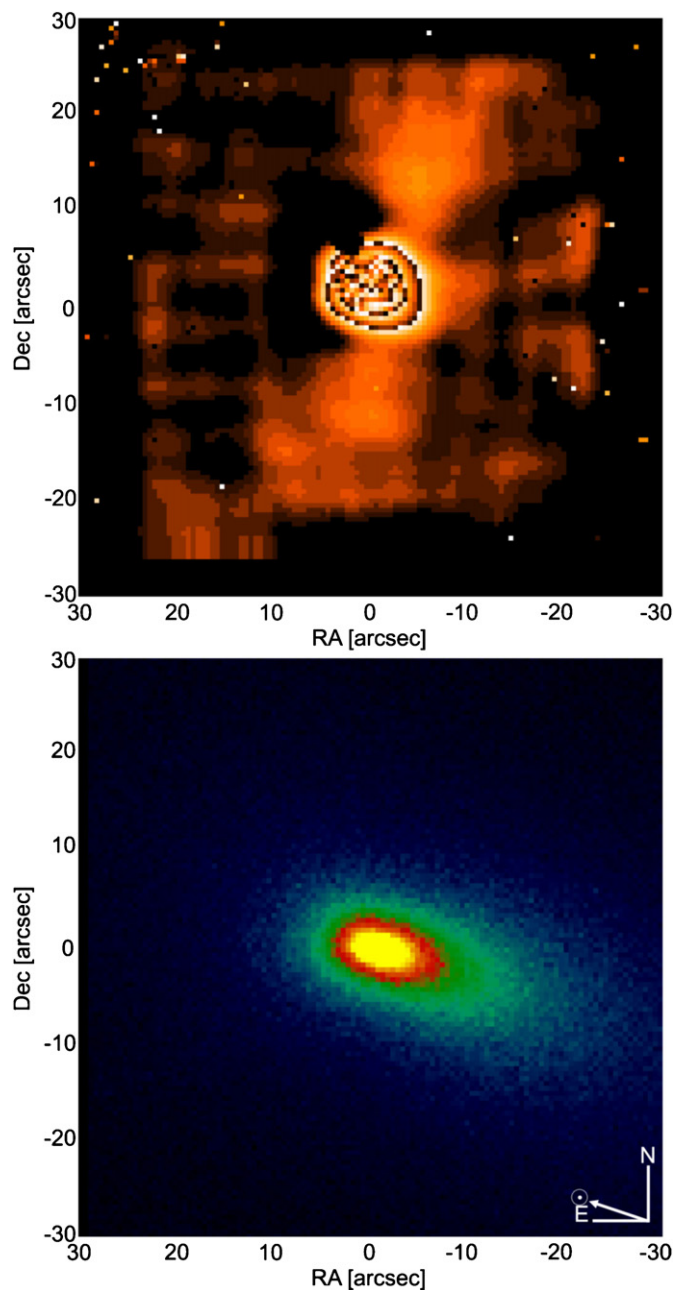


Figure 10. Comparison between CN structures and dust in fragment C. Top: adaptive Laplace filtering method of the CN image in Figure 8 (bottom). Bottom: optical images using the ESA Rosetta comet filters for the blue continuum at 445/4 nm.

(A color version of this figure is available in the online journal.)

to a steady-state model) is needed to evaluate if the HCN and CN production rates for fragment B are consistent with HCN as the sole source or not. This model is beyond the scope of this paper, but clearly a proper interpretation of the HCN–CN link in the case of impulsive events (e.g., in fragment B) requires such a model before suggesting alternative sources for cyanide.

Similar to Woodney et al. (2002), we also observe large variation in rates for CN production in fragment B. Among others, these undesired effects are mostly introduced by uncertainties in model parameters, such as CN lifetimes and scale lengths, which are not accurately known. As a result, a conclusion suggesting similar production rates for HCN and CN is certainly constrained by the model parameters assumed in our calcu-

lations. Upcoming studies by other observers would provide complementary information to establish any further conclusion. Indeed, we note a lack of published CN/H₂O abundances on 2006 May 12. For instance, a report of CN/H₂O abundances at optical wavelengths resulted in 0.28% and 0.20% for fragments B and C on May 14, respectively (Kanda et al. 2008). These estimations are in accordance with HCN/H₂O abundances at IR wavelengths on the same day (Dello Russo et al. 2007).

In addition to an equivalent outgassing production and a similar morphological structure of the observed species, a full analysis of HCN–CN parentage requires the determination (and agreement) of the parent photodissociation scale length and the daughter formation scale length (as was mentioned above). In our case, the intrinsic limitations of our observations make difficult the retrieval of reliable scale lengths for comet 73P, ultimately preventing us to rule out alternative mechanisms for cyanide production.

Last but not least, it is important to remark the large fluctuation encountered in the chemical taxonomy among different comets (even in the same nucleus as observed by Deep Impact; Mumma et al. 2005; Feaga et al. 2007); this suggests that comets underwent complex thermochemical processes at different regions within the protoplanetary disk (Morbidelli et al. 2008). As it was mentioned, several investigations about the relation of hydrogen cyanide with CN have guided astronomical observers to a wide variety of conclusions. In particular, some studies have established hasty conclusions based on a particular observed comet. The large chemical diversity encountered in cometary composition, however, clearly indicates that more evidence is required to put some light into this debate, most probably on a statistical basis.

6. CONCLUSIONS

Parent volatiles released by the nucleus were analyzed by means of their rotational transitions at millimeter wavelengths. These allowed us to provide HCN production rates for fragments B and C, and thus their gas evolution, at heliocentric distances between 0.966 and 1.033 AU before perihelion. Furthermore, our observations provided unprecedented coverage shortly after the observed increase in outgassing activity of fragment B, estimated to have happened on 2006 May 8–9. During these days, outgassing ejecta enhanced gas productivity in 73P-B surpassing that of fragment C—a behavior which was not observed previously during 73P's apparition in 2006 and that finished ~8 days later according to our estimations.

In addition, we have discussed the role of HCN and dust as parent sources for CN, and the potential synergy between observations at different wavelengths. This study suggests a high correlation between HCN and CN, rather than an origin from a grain source, and thus supports previous investigations indicating HCN as a major source for CN (provided that we only consider analysis of jet morphologies and production rates). Nevertheless, the presence of an alternative source for cyanide could not be fully ruled out. Clearly, the larger sensitivity and spatial resolution attained by upcoming interferometers, such as ALMA, will certainly enhance previous studies and provide some light into this discussion.

This work is based on joint observations from the Heinrich Hertz Submillimeter Telescope and Lulin Observatory. We are grateful to the staff of HHSMT and LO for their great assistance and generous allocation of telescope time throughout

our observational campaign. L.P. acknowledges D. Bockelée-Morvan, N. Biver, K. Jockers, M. Drahus, M. Lippi, and M. J. Mumma for useful discussions, the anonymous referee for valuable comments on the manuscript, and the support of this research by the Max-Planck-Gesellschaft. L.M.L. and Z.-Y.L. thank the support given by the Spanish Ministerio de Educación y Ciencia and Ministerio de Ciencia e Innovación under projects ESP2006-02934 and AyA 2009-08011. The SMT is operated by the Arizona Radio Observatory (ARO), Steward Observatory, University of Arizona.

REFERENCES

- A'Hearn, M. F., Millis, R. L., Schleicher, D. G., Osip, D. J., & Birch, P. V. 1995, *Icarus*, **118**, 223
- Baars, J. W. M., Martin, R. N., Mangum, J. G., McMullin, J. P., & Peters, W. L. 1999, *PASP*, **111**, 627
- Bensch, F., & Bergin, E. A. 2004, *ApJ*, **615**, 531
- Bertini, I., Lara, L. M., Vincent, J.-B., Boehnhardt, H., Küppers, M., & Rodrigo, R. 2009, *A&A*, **496**, 235
- Biver, N. 1997, PhD thesis, Univ. Paris VII
- Biver, N., et al. 1999, *AJ*, **118**, 1850
- Blake, G. A., Qi, C., Hogerheijde, M. R., Gurwell, M. A., & Muhleman, D. O. 1999, *Nature*, **298**, 213
- Bockelée-Morvan, D., Crovisier, J., Mumma, M. J., & Weaver, H. A. 2004, in *Comets II*, ed. M. C. Festou, H. U. Keller, & H. A. Weaver (Tucson, AZ: Univ. Arizona Press), 391
- Bockelée-Morvan, D., et al. 1984, *A&A*, **141**, 411
- Bockelée-Morvan, D., et al. 1985, *A&A*, **151**, 90
- Bockelée-Morvan, D., et al. 2000, *A&A*, **353**, 1101
- Bockelée-Morvan, D., et al. 2008, *ApJ*, **679**, L49
- Bönhardt, H., Kaufl, H. U., Keen, R., Camilleri, P., Carvajal, J., & Hale, A. 1995, *IAU Circ.*, **6274**, 1
- Boissier, J., Bockelée-Morvan, D., Biver, N., Crovisier, J., Despois, D., Marsden, B. G., & Moreno, R. 2007, *A&A*, **475**, 1131
- Bonev, B. P., Mumma, M. J., Kawakita, H., Kobayashi, H., & Villanueva, G. L. 2008a, *Icarus*, **196**, 241
- Bonev, B. P., Mumma, M. J., Radeva, Y. L., DiSanti, M. A., Gibb, E. L., & Villanueva, G. L. 2008b, *ApJ*, **680**, L61
- Combi, M. R., et al. 1999, *ApJ*, **512**, 961
- Crovisier, J. 1984, *A&A*, **130**, 361
- Crovisier, J., & Encrenaz, Th. 1983, *A&A*, **126**, 170
- Dello Russo, N., Vervack, R. J., Weaver, H. A., Biver, N., Bockelée-Morvan, D., Crovisier, J., & Lisse, C. M. 2007, *Nature*, **448**, 172
- de Pater, I., et al. 1998, *AJ*, **116**, 987
- Drahus, M., Küppers, M., Jarchow, C., Paganini, L., Hartogh, P., & Villanueva, G. L. 2010, *A&A*, **510**, 55
- Faure, A., et al. 2007, *MNRAS*, **382**, 840
- Feaga, L. M., et al. 2007, *Icarus*, **190**, 284
- Fray, N., Bénilan, Y., Cottin, H., Gazeau, M.-C., & Crovisier, J. 2005, *Planet. Space Sci.*, **53**, 1243
- Friedel, D. N., et al. 2005, *ApJ*, **630**, 623
- Fuse, T., et al. 2007, *PASJ*, **59**, 381
- Haser, L. 1957, *Bull. Soc. R. Sci. Liege*, **43**, 740
- Hogerheijde, M. R., & van der Tak, F. F. S. 2000, *A&A*, **362**, 697
- Huebner, W. F. Keady, J. J., & Lyon, S. P. 1992, *Ap&SS*, **195**, 1
- Jones, T. J., et al. 2008, *AJ*, **135**, 1318
- Kanda, Y.-i., Mori, A., Kobayashi, H., & Kawakita, H. 2008, *PASJ*, **60**, 1191
- Kinoshita, D., et al. 2005, *Chin. J. Astron. Astrophys.*, **5**, 315
- Kobayashi, H., Kawakita, H., Mumma, M. J., Bonev, B. P., Watanabe, J., & Fuse, T. 2007, *ApJ*, **668**, L75
- Lin, Z. Y., et al. 2007, *A&A*, **469**, 771
- Lin, Z. Y., et al. 2009, *AJ*, **138**, 625
- Lis, D. C., et al. 2008, *ApJ*, **675**, 931
- Lovell, A. J., et al. 1999, *Earth Moon Planets*, **77**, 253
- Manfroid, J., et al. 2005, *A&A*, **432**, L5
- Morbidelli, A., Levison, H. F., & Gomes, R. 2008, in *The Solar System Beyond Neptune*, ed. M. A. Barucci, H. Boehnhardt, D. P. Cruikshank, & A. Morbidelli (Tucson, AZ: Univ. Arizona Press), 275
- Mumma, M. J., et al. 2005, *Science*, **310**, 270
- Newburn, R. L., & Spinrad, H. 1989, *AJ*, **97**, 552
- Pickett, H. M., Poynter, R. L., Cohen, E. A., Delitsky, M. L., Pearson, J. C., & Muller, H. S. P. 1998, *J. Quant. Spectrosc. Radiat. Transfer*, **60**, 883
- Reach, W. T., et al. 2009, *Icarus*, **203**, 571

- Rothman, L. S., et al. 2009, *J. Quant. Spectrosc. Radiat. Transfer*, **110**, 533
- Sault, R. J., Teuben, P. J., & Wright, M. C. H. 1995, in ASP Conf. Ser. 77, *Astronomical Data Analysis Software and Systems IV*, ed. R. A. Shaw, H. E. Payne, & J. J. E. Hayes (San Francisco, CA: ASP), 433
- Schleicher, D. G. 1983, PhD thesis, Univ. Maryland
- Ulich, B. L., & Haas, R. W. 1976, *ApJS*, **30**, 247
- Veal, J. M., et al. 2000, *AJ*, **119**, 1498
- Villanueva, G. L., et al. 2006, *ApJ*, **650**, L87
- Vincent, J.-B., Bönnhardt, H., Bertini, I., Lara, L.-M., Küppers, M., & Rodrigo, R. 2010, *Earth Moon Planets*, **106**, 27
- Waniak, W., Borisov, G., Drahus, M., Bonev, T., Czart, K., & Küppers, M. 2009, *Earth Moon Planets*, **105**, 327
- Weaver, H. A., & Mumma, M. J. 1984, *ApJ*, **276**, 782
- Wink, J., et al. 1999, *Earth Moon Planets*, **78**, 63
- Woodney, L. M., et al. 2002, *Icarus*, **157**, 193
- Wright, M. C. H., et al. 1998, *AJ*, **116**, 3018
- Xie, X., & Mumma, M. J. 1992, *ApJ*, **386**, 720